Zinc surface complexes on birnessite: A density functional theory study

Kideok D. Kwon[1*], Keith Refson[2], and Garrison Sposito[1]

[1]Geochemistry Department, Earth Sciences Division, Lawrence Berkeley National Laboratory, Berkeley, CA 94720

[2]STFC Rutherford Appleton Laboratory, Didcot, Oxfordshire OX11 0QX, United Kingdom

*Corresponding author: kkwon@nature.berkeley.edu

Abstract

Biogeochemical cycling of zinc is strongly influenced by sorption on birnessite minerals (layer-type MnO_2), which are found in diverse terrestrial and aquatic environments. Zinc has been observed to form both tetrahedral (Zn^{IV}) and octahedral (Zn^{VI}) triple-corner-sharing surface complexes (TCS) at Mn(IV) vacancy sites in hexagonal birnessite. The octahedral complex is expected to be similar to that of Zn in the Mn oxide mineral, chalcophanite ($ZnMn_3O_7 \cdot 3H_2O$), but the reason for the occurrence of the four-coordinate Zn surface species remains unclear. We address this issue computationally using spin-polarized Density Functional Theory (DFT) to examine the Zn^{IV}-TCS and Zn^{VI}-TCS species. Structural parameters obtained by DFT geometry optimization were in excellent agreement with available experimental data on Zn-birnessites. Total energy, magnetic moments, and electron-overlap populations obtained by DFT for isolated Zn^{IV}-TCS revealed that this species is stable in birnessite without a need for Mn(III) substitution in the octahedral sheet and that it is more effective in reducing undersaturation of surface O at a Mn vacancy than is Zn^{VI}-TCS. Comparison between geometry-optimized $ZnMn_3O_7 \cdot 3H_2O$ (chalcophanite) and the hypothetical monohydrate mineral, $ZnMn_3O_7 \cdot H_2O$, which contains only tetrahedral Zn, showed that the hydration state of Zn significantly affects birnessite structural stability. Finally, our study also revealed that, relative to their positions in an ideal vacancy-free MnO_2, Mn nearest to Zn in a TCS surface complex move toward the vacancy by 0.08 – 0.11 Å, while surface O bordering the vacancy move away from it by 0.16 – 0.21 Å, in agreement with recent X-ray absorption spectroscopic analyses.

1. INTRODUCTION

Birnessite (layer-type MnO_2), produced mainly by bacteria and fungi, is a ubiquitous environmental nanoparticle participating in important geochemical processes, particularly metal scavenging (Tebo et al., 2004; Tonkin et al., 2004; Toner et al., 2006, Manceau et al., 2007; Miyata et al., 2007). Among the trace metals of major interest, Zn appears to be influenced strongly in its biogeochemical cycling by sorption on birnessite minerals found in soils, aquifers, streams, and wetlands (Toner et al., 2006). Detailed molecular-scale studies of sorbed Zn^{2+} species have been published for chemically- and microbially-synthesized birnessite (Manceau et al., 2002; Toner et al., 2006), natural soil and marine birnessite (Marcus et al., 2004; Manceau et al., 2007), and Zn-Mn coprecipitates on plant roots (Lanson et al., 2008). These studies reveal that Zn^{2+} binds to Mn(IV) vacancy sites in hexagonal birnessite, forming triple-corner-sharing (TCS) inner-sphere surface complexes with the three surface O surrounding a vacancy. This mode of binding is similar to that observed in the mineral, chalcophanite [$ZnMn_3O_7 \cdot 3H_2O$, Post and Appleman (1988)], in which Zn is in octahedral coordination with three surface O around a Mn(IV) vacancy as well as three O from three structural H_2O (Fig. 1). However, the local coordination environment of Zn sorbed by birnessite does not merely replicate that in chalcophanite. Manceau et al. (2002) have shown that, in addition to octahedrally-coordinated Zn (Zn^{VI}-TCS), tetrahedrally-coordinated Zn (Zn^{IV}-TCS) bound to three surface O and one H_2O can exist in Zn-birnessite, preferentially at low surface coverage of Zn. Structural parameters reported for their sample ZnBi8, i.e., nearest-neighbor distances, d(Zn-O) = 1.97 Å and d(Zn-Mn_{1st}) = 3.35 Å, and a Zn-O coordination number near 4, are representative of the Zn^{IV}-TCS species (Table 1).

Among the studies of Zn sorbed on birnessite summarized in Table 1 none describes a fully-characterized reference sample suitable for use as a unique Zn^{IV}-TCS end-member. The synthetic birnessite for which Manceau et al. (2002) first reported the presence of Zn^{IV}-TCS contained about 13 mol % Mn(III) substituted for Mn(IV) in the octahedral sheet (Lanson et al., 2002), and the formation of Zn^{IV}-TCS was accordingly conjectured to result from the presence of this structural Mn(III) (Manceau et al., 2002). Similarly, the natural marine Zn-birnessite sample investigated by Marcus et al. (2004), whose octahedrally-coordinated Zn content is at most 7 mol %, was reported to have about 10 mol % Mn(III) substituted in the octahedral sheet. However, other birnessite samples shown to contain the Zn^{IV}-TCS species comprise sheets of octahedra with only Mn(IV) present [sediment birnessite, Isaure et al. (2005); bacteriogenic birnessite and δ-MnO_2, Toner et al. (2006); quartz-coating birnessite, Manceau et al. (2007); plant-root Zn-Mn coprecipitate, Lanson et al. (2008)]. Therefore, it does not seem necessary to connect the existence of Zn^{IV}-TCS uniquely to the presence of Mn(III) substituted in the octahedral sheet and the fundamental basis for the occurrence of the four-coordinate surface species remains unclear.

In the present paper, we address this conundrum theoretically using geometry optimizations based on Density Functional Theory (DFT) to examine the Zn^{IV}-TCS and Zn^{VI}-TCS species in hexagonal layer-type $Mn(IV)O_2$. First-principles simulations based on DFT can describe chemical bonding features of condensed phases, such as minerals, to a high degree of accuracy without adjustable parameters (Koch and Holthausen, 2002; Cramer, 2003; Martin, 2004; Kohanoff, 2006). These simulations thus complement experimental data by exploring electronic and structural details of complex systems which experimental techniques may not

fully elucidate. In the present case, hydrated Zn surface complexes were geometry-optimized via total energy and force minimization to provide detailed structural and electronic information about their stable groundstates. Density functional theory using plane-wave basis sets and periodic boundary conditions subject to Bloch's Theorem (Payne et al., 1992; Segall et al., 2002) is especially well-positioned to achieve accurate results for layer-type minerals through careful convergence tests performed by systematically varying the DFT components [e.g., kinetic energy cutoff, Brillouin zone sampling, and supercell size (Mattsson et al., 2005)]. Furthermore, since a plane-wave basis set treats empty space the same as it does the atoms on a lattice, defect structures such as Mn(IV) vacancies are described without structural bias.

To validate the quality of our DFT calculations, as well as examine the stability of hexagonal Zn-Mn(IV)O_2, we first geometry-optimized the structure of chalcophanite ($ZnMn_3O_7 \cdot 3H_2O$) and compared our results to available experimental data. Then an isolated Zn^{IV}-TCS complex at a Mn(IV) vacancy was examined as a Zn^{IV}-TCS end-member. Lastly, doubly-occupied Zn-TCS complexes (i.e., Zn^{IV}-TCS + Zn^{IV}-TCS; Zn^{VI}-TCS + Zn^{VI}-TCS; Zn^{IV}-TCS + Zn^{VI}-TCS) were considered by analogy with the double Zn occupancy found in chalcophanite. Structural distortion of a Mn(IV) vacancy site was also investigated to understand why interatomic distances determined by X-ray absorption spectroscopy often are not compatible with those determined by X-ray diffraction, with reconciliation between the two then requiring ad hoc displacement of the surface O positions around a vacancy (Manceau et al., 2002; Villalobos et al., 2005; Lanson et al., 2008).

2. COMPUTATIONAL DETAILS

2.1. Spin-polarized plane-wave DFT

All DFT optimizations were performed with the CASTEP code (Clark et al., 2005), which implements DFT in a plane-wave basis set to represent wavefunctions and uses ultrasoft pseudopotentials to replace strong coulomb potentials between atomic nuclei and core electrons with weak effective potentials, thus dramatically reducing the number of plane waves required to represent wavefunctions. Under standard approximations to account for electron exchange and correlation, eigenstates and eigenvalues of the Kohn-Sham Schrödinger equations (Kohn and Sham, 1965) were solved via efficient self-consistent iterative methods including density mixing (Kresse and Furthmüller, 1996). The CASTEP code has proven to be of very high accuracy in condensed matter studies (Milman et al., 2000), approaching the accuracy of all-electron (AE) methods, and of high efficiency in large-scale calculations such as solid-state defect studies (Probert and Payne, 2003).

Electron exchange and correlation were treated under the generalized gradient approximation (GGA) using Perdew, Burke, and Ernzerhof (PBE) functionals (Perdew et al., 1996). Ultrasoft pseudopotentials (Vanderbilt, 1990) were constructed for Mn and O ions using the on-the-fly pseudopotential generator implemented in CASTEP with the valence-electron configurations $3s^2 3p^6 3d^5 4s^2$ for Mn and $2s^2 2p^4$ for O. The core radius for Mn was 2.3 a_0 (a_0 = 0.52918 Å is the Bohr radius) while that of O was 1.3 a_0. The q_c for KE optimization were set at 5.5 and 6 a_0^{-1} for Mn and O, respectively. Tests of the ultrasoft pseudopotentials at a 500 eV cut-off energy reproduced structure and energy data of MnO as calculated with AE methods (Pask et al., 2001). For H and Zn ($3d^{10} 4s^2$, core radius = 2.0 a_0), Vanderbilt ultrasoft pseudopotentials in the CASTEP library were used (version 7.3.2). Test runs on ZnO in the wurtzite structure and

aqueous Zn in the form of $[Zn(H_2O)_4]^{2+}\bullet(H_2O)_2$ and $[Zn(H_2O)_6]^{2+}$ also reproduced the results of AE calculations (Dudev and Lim, 2000; Zhao et al., 2006).

The electrons in Mn ions are spin-polarized (i.e., unequal numbers of spin-up and spin-down electrons occupy the orbitals), leading to a net magnetic moment and thus magnetic coupling between Mn ions. Accordingly, to reproduce accurately the structural, electronic, and magnetic properties of Mn oxides, a spin-polarization treatment is essential in performing DFT calculations (Balachandran et al., 2003; Pask et al., 2001; Singh, 1997), i.e., electron densities are calculated separately for spin-up and spin-down orientations. All calculations in the present study were performed with spin polarization and exhibited ferromagnetic ordering among Mn ions within a layer. [The triangular Mn lattice does not allow an antiferromagnetic spin order because of frustration (Moessner and Ramirez, 2006), resulting in the stabilization of the otherwise higher energy ferromagnetic ordering.] Calculations for vacancy-free MnO_2 showed that omitting spin polarization underestimated important interatomic distances as much as by 0.1 Å as compared to the corresponding spin-polarized calculations, a result which is consistent with those of Mishra and Ceder (1999) as well as with available experimental data. Antiferromagnetic alignment between octahedral sheets with ferromagnetic ordering in each sheet was also examined as an alternative, but the total energy difference found was less than the energy variability in calculations using the chosen approach (0.005 eV/Å).

2.2. Model structures

The hexagonal unit cell reported by Post and Appleman (1988) was used as a starting structure for geometry optimization of chalcophanite ($ZnMn_3O_7\cdot 3H_2O$). For the Zn-TCS species

in birnessite, a model hexagonal $Mn(IV)O_2$ with Mn(IV) vacancies charge-compensated by protons was developed as follows: First, vacancy-free $Mn(IV)O_2$ was geometry-optimized based on the Mn and O atomic coordinates of microcrystalline layer-type K-$Mn(IV)O_2$ (Gaillot et al., 2003). This well-characterized Mn oxide has space group $P6_3/mmc$ and a two-layer unit cell with hexagonal lattice parameters a = 2.840 Å and c = 14.031 Å. Second, a protonated defect was introduced into a 4 x 4 x 1 supercell of vacancy-free MnO_2 by coordination of one Mn vacancy at the center of the supercell to four H bound to the "dangling" O ions bordering the vacancy. This supercell corresponds to the structural formula, $H_{0.13}[Mn_{0.967}\square_{0.033}]O_2$, where $\square$ represents a vacancy. The protonated 4 x 4 x 1 MnO_2 supercell was geometry-optimized using a 500 eV cut-off energy and a 2 x 2 x 1 *k*-point grid for the first Brillouin zone (Monkhorst and Pack, 1976) after fixing the three unit-cell angles (90º, 90º, and 120º) and the c lattice parameter (14.001 Å, as obtained for the geometry-optimized vacancy-free MnO_2), but with the a and b lattice parameters and all internal ionic positions relaxed under 0.01 eV/Å and 0.02 GPa tolerance for the maximum force and stress, respectively, along any Cartesian component. Lastly, in the geometry-optimized protonated MnO_2 supercell (i.e., 11.587 Å x 11.587 Å x 14.001 Å), either two or four H at the vacancy site were replaced with either one or two Zn^{2+} ions coordinated to H_2O molecules to give the composition $Zn_x(H_2O)_n{\cdot}H_{4-2x}[Mn_{31}\square]O_{64}$ (x = 1 or 2, n = 1 or 3) for singly-occupied (x = 1), or doubly-occupied (x = 2), Zn^{IV}-TCS (n = 1) or Zn^{VI}-TCS (n = 3). Thus the charge deficit created by a Mn(IV) vacancy was compensated either by one Zn-TCS species and two H on the other side of the sheet or by two Zn-TCS species on both sides.

2.3. Geometry optimizations

Geometry optimizations were performed without imposed symmetry using the Broyden, Fletcher, Goldfarb, Shanno (BFGS) procedure (Pfrommer et al., 1997). [The damped molecular dynamics method (Probert, 2003) was also explored, but significant improvement was not observed as compared to the BFGS method.] The energy tolerance was 5 x 10^{-6} eV/atom, and the maximum tolerance for force and for atom displacement along any Cartesian component was 0.03 eV/Å and 0.0005 Å, respectively. In an effort to obtain an accurate force, low tolerance was used for the self-consistent-field electronic energy (10^{-8} eV/atom).

In the geometry optimization of $ZnMn_3O_7 \cdot 3H_2O$, all internal atomic positions and lattice parameters were relaxed on a 4 x 4 x 1 *k*-point grid (i.e., eight *k*-points) for the first Brillouin zone with a 500 eV cut-off energy for the ultrasoft pseudopotentials. Convergence tests performed for the 4 x 4 x 1 *k*-point grid showed very high convergence of force (0.001 eV/Å or better). In addition to the total energy and force, the CASTEP code calculates the stress tensor of a model system during geometry optimization. The root-mean-square (RMS) value of the calculated stress tensor can be used to evaluate the quality of a geometry optimization, in particular for supercells, because the ideal value for a groundstate crystal geometry-optimized under zero pressure should be close to 0 GPa. In our optimized chalcophanite model, the RMS stress was only 0.002 GPa.

For Zn-TCS-MnO_2, all internal ionic positions in the 4 x 4 x 1 supercell were relaxed with fixed lattice parameters (i.e., 11.587 Å x 11.587 Å x 14.001 Å and 90º, 90º, and 120º). Relaxation of the lattice parameters did not affect the precision of our results in terms of the interatomic distances: the RMS stress of the optimized Zn^{IV}-TCS + Zn^{VI}-TCS MnO_2 supercell was 0.253 GPa, and further relaxation of the lattice parameters to yield a RMS stress of 0.058

GPa (i.e., 11.570 Å x 11.570 Å x 14.131 Å and 90º, 90º, and 120º) showed a tendency to increase the interatomic distances by no more than 0.005 Å. The RMS stress of the optimized Zn^{IV}-TCS-MnO_2 model was 0.158 GPa. For the first Brillouin zone of the Zn-TCS-MnO_2, a 2 x 2 x 2 *k*-point grid (i.e., four *k*-points) was used without offset of the grid origin. Convergence tests performed for the 2 x 2 x 2 *k*-point grid with a 500 eV cut-off energy showed very high convergence of force (0.005 eV/Å or better).

In an insufficiently large supercell, interactions between a Zn ion and its images in neighboring periodic cells could result in significant errors in the calculated total energy and force, and hence inaccurate geometry-optimized isolated Zn-TCS structures. To estimate the influence of MnO_2 supercell size, geometry-optimized distances between Zn and unsaturated surface O (Zn-O_{2Mn}) were compared among the Zn-TCS-MnO_2 supercells (without H_2O), 2 x 2 x 1 (i.e., 5.793 Å x 5.793 Å x 14.001 Å with 7 Mn and 16 O atoms), 4 x 4 x 1 (i.e., 11.587 Å x 11.587 Å x 14.001 Å with 31 Mn and 64 O atoms), and 6 x 6 x 1 (i.e., 17.380 Å x 17.380 Å x 14.001 Å with 71 Mn and 144 O atoms). During these geometry optimizations, only the Zn position was relaxed, and all Mn and O positions were fixed based on the vacancy-free MnO_2 structure with the same plane-wave cut-off energy (500 eV) and the equivalent *k*-point grid density (e.g., 4 x 4 x 2 *k*-point grid for the 2 x 2 x 1 supercell). The Zn-O distances found in these tests were 1.830 Å, 1.837 Å, and 1.839 Å for the 2 x 2 x 1, 4 x 4 x 1, and 6 x 6 x 1 supercells, respectively. Because the Zn-O distance tends to converge well for the 4 x 4 x 1 supercell, it was regarded sufficiently large to minimize the unwanted interactions between Zn-TCS-MnO_2 cells.

2.4. Magnetic moments and electron overlap population analysis

Determining the oxidation states of Mn ions in birnessites remains an important research challenge (Kim et al., 1999; Manceau et al., 2002; Gaillot et al., 2003). Bond valence sums (Manceau et al., 2002) associated with X-ray diffraction modeling (Villalobos et al., 2006) provide semi-quantitative values, but magnetic moments or orbital-projected density of states in conjunction with crystal-field theory can give better information. For example, because the magnetic moments based on Hund's rule for isolated high-spin Mn(IV) and Mn(II) are 3 μ_B and 5 μ_B, respectively ($\mu_B = 9.274 \times 10^{-24}$ J T^{-1} is the Bohr magneton), magnetic moments can indicate the oxidation numbers of Mn ions. Magnetic moments were calculated to identify the oxidation states of Mn in chalcophanite and in the Zn-TCS-MnO_2 models through electron population analysis as implemented in CASTEP (Segall et al., 1996). Because unsaturated surface O ions of metal oxides show a large induction effect on spin polarization as compared to saturated O (Cline et al., 2000; Gallego et al., 2005), the spin states of O ions were analyzed to determine the relative bonding saturation of O near a Mn vacancy in Zn^{IV}-TCS vs. Zn^{VI}-TCS. Population analysis, in which plane-wave eigenfunctions are projected on to pseudo-atomic basis sets using the Mulliken formalism (Mulliken, 1955), also provides the number of electrons overlapped between ions, allowing correlation of the overlap population with the bond strength (Segall et al., 1996). Thus the overlap population between Zn and O was analyzed to evaluate a relative bond strength for Zn^{IV}-TCS vs. Zn^{VI}-TCS. The difference between the plane-wave eigenfunctions and the projected orbitals, which represents the incompleteness of the Mulliken analysis, was only 0.20 to 0.22 %.

3. RESULTS AND DISCUSSION

3.1. $ZnMn_3O_7 \cdot 3H_2O$

3.1.1. Geometry-optimized structure

Negligible differences were found between the calculated DFT and experimental atomic coordinates for chalcophanite, except for the structural H_2O molecules (Table 2). However, the DFT-calculated distance between Zn and the nearest Mn in an adjacent sheet was 5.32 Å, which is much longer than the experimental value of 5.14 Å. Constrained geometry optimization performed with the *c* parameter fixed at the XRD value (i.e., relaxation of all ionic positions, angles, and lattice parameters except for c = 20.794 Å) decreased the calculated distance to 5.18 Å without significant changes in the other interatomic distances. Therefore, the larger *c* parameter predicted by the fully-relaxed $ZnMn_3O_7 \cdot 3H_2O$ optimization can be attributed simply to overestimation of the interlayer spacing between octahedral sheets by DFT/GGA.

Structural parameters describing the local Zn coordination environment were in excellent agreement with experiment. For example, the DFT bond length between Zn and surface O [d(Zn-O_{2Mn}), where O_{2Mn} is O coordinated with two Mn] was 2.07 Å (Fig. 1a) as compared to experimental values of 2.07 Å (XRD, Post and Appleman, 1988) and 2.04 Å (EXAFS, Manceau et al., 2002), while the DFT distance between Zn and the O of H_2O [d(Zn-O(H_2O))] was slightly larger (2.24 Å) than the corresponding XRD (2.14 Å) and EXAFS (2.16 Å) values. The DFT distance between Zn and the nearest Mn [d(Zn-Mn_{1st})] was 3.51 – 3.52 Å (Fig. 1b), which is consistent with the results of XRD (3.49 – 3.50 Å) and EXAFS (3.52 Å) measurements.

According to the results of our optimization, structural H_2O in chalcophanite are oriented such that one H (H1) points toward an adjacent sheet while the other H (H2) forms a H-bond with a H_2O hydrating a neighboring Zn (Fig. 1a). The DFT-calculated H-bond distance between

H1 and O_{2Mn} was 2.19 Å and that between H1 and O_{3Mn} was 2.24 to 2.49 Å. The H-bond distance between H2 and O of H_2O coordinated to a neighboring Zn was 1.80 Å. Thus the H-bond distances between H_2O molecules hydrating neighboring Zn are much shorter than those with the octahedral sheet, as also found by Post and Appleman (1988) [H1…O_{2Mn}: 2.11 Å; H1…O_{3Mn}: 2.19 – 2.41 Å; H2…O(H_2O): 1.98 Å] using a modified-electron gas approach (Cohen and Gordon, 1976) constrained by the fixed chalcophanite structure as obtained by XRD refinement. Although the DFT-calculated H-bond distance between H_2O molecules is much shorter than that calculated by Post and Appleman (1988), the calculated distance between O of the H-bonded H_2O molecules (2.76 Å) is very close to their XRD result (2.77 Å).

3.1.2. Stabilizing effect of intermolecular H-bonds

The effects of intermolecular H_2O-H_2O H-bonds of Zn complexes on chalcophanite stability was examined by comparison of the geometry-optimized structures of $ZnMn_3O_7 \cdot 3H_2O$ and a hypothetical monohydrate, $ZnMn_3O_7 \cdot H_2O$, which contains tetrahedrally-coordinated Zn created by removal of two H_2O in the trihydrate $ZnMn_3O_7 \cdot 3H_2O$ and, therefore, has no H-bonds between neighboring Zn complexes. To reduce computation time, a rhombohedral primitive cell of chalcophanite was fully geometry-optimized without imposed symmetry instead of a hexagonal unit cell (e.g., 18 Mn in a hexagonal cell vs. 6 Mn in a rhombohedral cell). The optimized cell parameters of $ZnMn_3O_7 \cdot 3H_2O$ were $a = b = c = 8.361$ Å and $\alpha = \beta = \gamma = 54.08°$, which are equivalent to the hexagonal parameters ($a = b = 7.602$ Å, $c = 21.349$ Å, and $\alpha = 90.0$, $\beta = 90.0$, $\gamma = 120.0°$). The hypothetical $ZnMn_3O_7 \cdot H_2O$ in a rhombohedral primitive cell was fully geometry-optimized without imposing symmetry, yielding the cell parameters $a = 8.891$, $b =$

8.160, c = 8.020 Å and α = 56.47°, β = 53.54°, γ = 53.08°; i.e., tetrahedral coordination of Zn lowered the trigonal Zn-MnO_2 to triclinic symmetry.

Although $ZnMn_3O_7 \cdot H_2O$ showed a typical range of Zn-O and Zn-Mn interatomic distances of Zn^{IV}, tetrahedral coordination of Zn significantly changed the birnessite structure in a manner similar to the translation of successive octahedral sheets that Manceau et al. (2002) and Lanson et al. (2002) have observed in Zn-MnO_2. In $ZnMn_3O_7 \cdot 3H_2O$, two Zn ions at a vacancy site are aligned with O_{3Mn} of a neighboring sheet (O3 in Table 2) to make a Zn-Zn-O3 angle of 180°. In $ZnMn_3O_7 \cdot H_2O$, the Zn ions are aligned with a tridentate cavity in the octahedral sheet to make a Zn-Zn-O3 angle of 167°; the apical O of H_2O is directed toward the O1-O3 edge in the tridentate cavity instead of toward O3. In the optimized $ZnMn_3O_7 \cdot H_2O$ structure, the separation between neighboring H_2O molecules was 3.65 Å, which is much larger than that in $ZnMn_3O_7 \cdot 3H_2O$ (2.76 Å), and the H-bonds between H_2O and a neighboring octahedral sheet (H…O1 and H…O3) were much shorter (1.71 to 2.10 Å) than the corresponding H-bonds in $ZnMn_3O_7 \cdot 3H_2O$ (2.19 to 2.49 Å).

This comparison made possible by DFT geometry optimization suggests that H-bonds are stabilized for octahedral Zn by linking the interlayer Zn through water molecules, whereas tetrahedral Zn stabilizes its H-bonds with adjacent octahedral sheets by altering the sheet registration to compensate for having no H-bonds between neighboring Zn. Johnson and Post (2006) recently have emphasized the importance of structural water molecules coordinated to interlayer metal cations in determining the stability of birnessite. The present study shows directly that the number of water molecules coordinated to interlayer metal cations in birnessite indeed strongly affects its structural integrity.

3.2. Isolated Zn^{IV}-TCS

3.2.1. Geometry-optimized structure

The geometry-optimized single Zn^{IV}-TCS yielded structural parameters in excellent agreement with available experimental results (Table 3). The average Zn-O and Zn-Mn_{1st} distances in the optimized Zn^{IV}-TCS were 1.96 and 3.34 Å, respectively, whereas the corresponding experimental distances for Zn^{IV}-TCS in the Zn-birnessite studied by Marcus et al. (2004) are 1.96 Å and 3.33 Å, respectively. In the geometry-optimized complex, the Zn ion was positioned about 0.72 Å above the basal O plane (Fig. 2a) and the H_2O molecule hydrating it formed H-bonds of length 1.95 and 1.97 Å with O_{3Mn} of a neighboring sheet. The calculated *d*(Mn-Mn) value was 2.83 to 2.94 Å, whereas the experimental *d*(Mn-Mn) is 2.89 ± 0.007 Å (Marcus et al., 2004). As in chalcophanite, *d*(Mn_{1st}-Mn_{1st}) was somewhat shorter (2.83 – 2.87 Å) than *d*(Mn_{1st}-Mn_{2nd}) (2.88 – 2.94 Å).

3.2.2. Stability of isolated Zn^{IV}-TCS

Manceau et al. (2002, 2007) have hypothesized that preference for Zn^{IV}-TCS in birnessite, particularly at a low Zn/Mn ratio, occurs because this complex compensates charge deficits on the unsaturated surface O (O_{2Mn}) at a Mn vacancy site more effectively than does Zn^{VI}-TCS. Our DFT optimizations allow a test of this hypothesis using the calculated magnetic moments of O_{2Mn} and the electron overlap population between Zn and O_{2Mn} (Section 2.4). In $ZnMn_3O_7 \cdot 3H_2O$, the calculated magnetic moment of O in a water molecule was 0.00 μ_B and the magnetic moment of O_{3Mn} was -0.04 to -0.06 μ_B, which is indistinguishable from zero. In the vacancy-free MnO_2 as

well as in the $H_{0.13}[Mn_{0.967}\square_{0.033}]O_2$ supercell with two H replaced by a Zn, the magnetic moment of O_{3Mn} was -0.04 μ_B. [A slightly negative spin polarization of *p* orbitals in non-magnetic elements like O typically occurs as a result of *p*-*d* hybridization in ferromagnetic transition metal compounds (Kanamori and Terakura, 2001)]. On the other hand, unsaturated O_{2Mn} without bonds with Zn or H (Fig. 2b) at a vacancy site took on a significant positive spin polarization, yielding a magnetic moment of + 0.12 μ_B. Considerable induction of positive spin polarization is typical of the outermost unsaturated surface O on metal oxides (Cline et al., 2000; Gallego et al., 2005). Therefore, our calculated magnetic moments of O indicate the degree of undersaturation of O_{2Mn} in Zn complexes.

Bond valence concepts predict that O_{2Mn} should be very reactive with cations (Manceau et al., 2002). When H is bonded to O_{2Mn} (i.e., Mn_2-O → Mn_2-O-H), our DFT calculations show that the magnetic moment of O_{2Mn} changes from + 0.12 μ_B to -0.04 μ_B, i.e. it becomes like that of saturated O_{3Mn}. Upon adsorption of Zn (i.e., Mn_2-O → Mn_2-O-Zn) to form Zn^{IV}-TCS, the magnetic moment of O_{2Mn} decreases to + 0.04 μ_B, and in Zn^{VI}-TCS (Fig. 3) it decreases to + 0.08 μ_B. (Moreover, in doubly-occupied Zn-TCS complexes, described in Section 3.3, the O_{2Mn} magnetic moment drops to + 0.02 μ_B in Zn^{IV}-TCS and to + 0.04 μ_B for Zn^{VI}-TCS, respectively.) Thus our DFT magnetic moment calculations show that formation of Zn^{IV}-TCS renders O_{2Mn} relatively more saturated than does formation of Zn^{VI}-TCS, a result which is consistent with the hypothesis of Manceau et al. (2002, 2007) concerning the relative stability of Zn^{IV}-TCS. The greater degree of electron overlap of Zn with O_{2Mn} in Zn^{IV}-TCS (0.36 |*e*|) than in Zn^{VI}-TCS (0.26 |*e*|) also supports this hypothesis.

Substitution of Mn(III) ions in the octahedral sheet also can lead to highly undersaturated basal O_{2Mn} and thus favor formation of Zn^{IV}-TCS relative to Zn^{VI}-TCS in birnessites (Manceau et al., 2002). However, our current DFT/GGA method was not able to test this mainly because of the over-delocalization tendency of DFT applied to electrons in mixed valence systems (Franchini, 2007). However, our DFT calculations do demonstrate that the stable existence of Zn^{IV}-TCS complexes in birnessite does not require the concomitant presence of Mn(III) ions in the MnO_2 sheets. As mentioned in Section 2.4, the magnetic moment of an ion can be used to infer its oxidation number [e.g., for isolated Mn(IV) it is 3 μ_B, for isolated Mn(III) it is 4 μ_B, and for isolated Mn(II) it is 5 μ_B.]. Our calculated magnetic moments of the Mn ions in the geometry-optimized reference compounds, $ZnMn(IV)_3O_7 \cdot 3H_2O$, $LiMn(III)O_2$, and Mn(II)O, were 3.08 μ_B, 3.86 μ_B, and 4.70 μ_B, respectively. The calculated magnetic moments of Mn in Zn^{IV}-TCS were all in the range of 3.00 to 3.08 μ_B, indicating therefore that all Mn ions are Mn(IV), as reported experimentally for δ-MnO_2 (Villalobos et al., 2006), biogenic Mn oxide (Toner et al., 2006), and natural vernadite (Manceau et al., 2007).

The stability of Zn^{IV}-TCS was examined by comparison of the total electronic energies of isolated Zn^{VI}-TCS and an isomer Zn^{IV}-TCS that has H-bonds with two neighboring H_2O [Zn^{IV}•$2H_2O$ (Fig. 3a)]. We found the total energy of Zn^{IV}-TCS to be slightly lower (by 11.6 kJ/mol) than that of Zn^{VI}-TCS (Fig. 3b). This energy comparison along with the magnetic moment and overlap analyses indicates that Zn^{IV}-TCS is indeed a stable species in hexagonal birnessite interlayers. We did not attempt calculation of the Gibbs energies of these two species (requiring zero-point energies, thermal energies, entropy contribution) or dynamic simulations with more hydrating H_2O molecules, both of which might provide more comprehensive

information on stability. Such a small difference in electronic energies between the two isolated isomers also suggests that Zn coordination can readily shift from tetrahedral Zn^{IV}-TCS to octahedral Zn^{VI}-TCS depending on external influences such as interactions with neighboring Zn (Section 3.1.2). Thus both Zn^{IV}-TCS and Zn^{VI}-TCS should be stable in birnessite.

3.3. Effects of Zn occupancy type

The value of *d*(Zn-O) did not vary significantly with the number of Zn species at a Mn vacancy site, but instead only with the Zn coordination number (Tables 3 and 4). However, the value of d(Zn-Mn_{1st}) did depend on Zn occupancy. Structural distortions around a Mn vacancy induced by the formation of Zn^{VI}-TCS + Zn^{VI}-TCS were exposed clearly by comparison to a constrained geometry-optimized structure of double-occupancy Zn-MnO_2 with fixed Mn and O positions (i.e., relaxation of only the two Zn and six H_2O during optimization, with the other atomic positions fixed at those in geometry-optimized vacancy-free MnO_2). [The poor prediction of d(Zn-Mn_{1st}), 3.51 – 3.68 Å, in the constrained structure emphasizes the importance of relaxation of the MnO_2 coordinates in geometry optimization.] When compared to the constrained structure, the fully-relaxed Zn^{VI}-TCS + Zn^{VI}-TCS structure revealed that Mn_{1st} move toward the vacancy by 0.08 – 0.11 Å, whereas O_{2Mn} move away from the vacancy by 0.16 – 0.21 Å (Fig. 4a). In order to interpret their EXAFS results, Manceau et al. (2002) postulated shifts of the O_{2Mn} positions outward from a vacancy by 0.15 Å relative to an undistorted birnessite structure based on XRD, and Villalobos et al. (2005) similarly postulated a 0.09 Å shift of O_{2Mn} positions outward from a vacancy in Pb-MnO_2.

These displacements of Mn_{1st} and O_{2Mn} can be understood readily in terms of cation repulsion and the screening of the cationic charge by O. Absence of one Mn cation out of three lessens the local repulsive energy, and it allows the surrounding Mn ions to contract about the vacancy, shortening the $d(Mn_{1st}\text{-}Mn_{1st})$ from 2.90 Å to 2.84 Å (Fig. 4b). At the same time, compensating O_{2Mn} displacement outward from the vacancy occurs to screen the cationic charge of the Mn_{1st} such that the angle $Mn_{1st}\text{-}O_{2Mn}\text{-}Mn_{1st}$ enlarges from 97.6° to 99.4 – 99.6°, the shared-edge length of Mn_{1st} octahedra [$d(O\text{-}O_{Mn1st})$] decreases from 2.54 Å to 2.52 Å, and that of vacant octahedron [$d(O\text{-}O_{vac})$] increases from 2.54 Å to 2.72 Å. Octahedral distortion includes significant variation in the distance between Mn and O [d(Mn-O)], from 1.93 Å to 1.86 – 1.97 Å.

Octahedrally-coordinated Zn has a larger radius than tetrahedrally-coordinated Zn, so octahedral Zn^{VI}-TCS + Zn^{VI}-TCS has a much larger separation of the two Zn through the vacancy [d(Zn-□-Zn)] than does tetrahedral Zn^{IV}-TCS + Zn^{IV}-TCS (4.17 Å vs. 3.34 Å, Fig. 5). The Zn cations in tetrahedral coordination thus exert more repulsion on nearby Mn, and hence the Mn_{1st} do not move inward as much as they do in the octahedral system: smaller movement by 0.04 – 0.05 Å in the former case, yielding $d(Mn_{1st}\text{-}Mn_{1st})$ = 2.88 Å (Fig. 4c) than in the latter case, yielding [$d(Mn_{1st}\text{-}Mn_{1st})$ = 2.84 Å (Fig. 4b)]. The O_{2Mn} move outward by 0.15 – 0.24 Å, which is slightly greater than in the octahedral system, with smaller $d(O\text{-}O_{Mn1st})$ (2.50 Å) and larger $d(O\text{-}O_{vac})$ (2.76 Å) (Fig. 4c). The value of d(Mn-O) was 1.89 – 1.95 Å.

Homogeneous Zn occupancy yields a homogeneous $d(Mn_{1st}\text{-}Mn_{1st})$ as a result of equivalent repulsions, mainly between Zn-TCS at the vacancy site (see the charge density of Zn-TCS in Fig. 5a, b). The mixed-occupancy structure Zn^{IV}-TCS + Zn^{VI}-TCS, however, shows two different $d(Mn_{1st}\text{-}Mn_{1st})$ values, 2.88 Å and 2.85 Å (Table 4), implying unequal electrostatic

interactions for the two types of Zn complex (Fig. 5c). The mixed-occupancy structure exhibits *d*(Zn-□-Zn) = 3.72 Å, which lies between the corresponding values for the homogeneous-occupancy structures (3.34 Å and 4.17 Å). In the mixed occupancy structure, the presence of octahedral Zn results in less repulsion of tetrahedral Zn than in Zn^{IV}-TCS + Zn^{IV}-TCS, thus decreasing *d*(Zn-Mn_{1st}) from 3.33 Å to 3.28 Å. Conversely, the presence of tetrahedral Zn results in more repulsion of the octahedral Zn than in Zn^{VI}-TCS + Zn^{VI}-TCS, thereby increasing *d*(Zn-Mn_{1st}) from 3.52 Å to 3.56 Å.

3.3.1. Zn^{IV}-TCS + Zn^{IV}-TCS

Our calculated *d*(Zn-Mn_{1st}) for Zn^{IV}-TCS + Zn^{IV}-TC (3.33 Å) is consistent with experimental values for tetrahedrally-coordinated Zn reported by Marcus et al. (2004) and Isaure et al.(2005) for natural birnessites (3.33 ± 0.02 Å) and by Toner et al. (2006) for a biogenic MnO_2 (3.36 ± 0.03 Å) and δ-MnO_2 (3.39 ± 0.02 Å). The angle between the Zn-Mn_{1st} pair and the octahedral sheet normal (β angle) was 59.1 – 60.2° and *d*(Zn-□-Zn) was 3.34 Å according to our DFT optimization (Fig. 5a). To interpret their polarized EXAFS data on a synthetic Zn-birnessite, Manceau et al. (2002) developed a structural model of Zn^{IV}-TCS + Zn^{IV}-TCS based on chalcophanite, wherein the β angle and *d*(Zn-□-Zn) were significantly different (56.4° and 3.54 Å, respectively) from our results, even though they fixed *d*(Zn-Mn_{1st}) at 3.35 Å. In the fully-relaxed $ZnMn_3O_7 \cdot H_2O$ optimization (Section 3.1.2), the β angle and *d*(Zn-□-Zn) were 58.6 – 59.3° and 3.50 Å, respectively, which are similar to the values of Manceau et al. (2002). These comparisons suggest that a tetrahedral Zn model developed with fixed chalcophanite coordinates may not accurately capture the detailed structure of Zn^{IV}-TCS found in Zn-birnessite.

3.3.2. Zn^{VI}-TCS + Zn^{VI}-TCS

In the geometry-optimized Zn^{VI}-TCS + Zn^{VI}-TCS structure, the value of d(Zn-Mn_{1st}) was 3.52 Å with β angle 53.5 – 54.1°, d(Mn_{1st}-Mn_{1st}) was 2.84 Å, and d(Zn-□-Zn) was 4.17 Å (Fig. 5b). The value of d(Zn-Mn_{1st}) agrees with experimental EXAFS data for octahedrally-coordinated Zn in biogenic MnO_2 (3.51 ± 0.02 Å), δ-MnO_2 (3.53 ± 0.02 Å), reported by Toner et al. (2006), and in chalcophanite (3.52 Å), reported by Manceau et al. (2002). The DFT β angle and d(Zn-□-Zn) value are both consistent with experimental XRD structural data for chalcophanite, whose β angle is 53.6° and d(Zn-□-Zn) value is 4.16 Å (Post and Appleman, 1988; Manceau et al., 2002).

3.3.3. Zn^{IV}-TCS + Zn^{VI}-TCS

In the mixed-occupancy structure (Fig. 5c), d(Zn-Mn_{1st}) for tetrahedral Zn was 3.28 Å (β angle = 60.5°), which is smaller than that in Zn^{IV}-TCS + Zn^{IV}-TCS (3.33 Å), while d(Zn-Mn_{1st}) for octahedral Zn was 3.56 Å (β angle = 53.2 – 53.7°), which is larger than that in Zn^{VI}-TCS + Zn^{VI}-TCS (3.52 Å). Although the DFT Zn-O distances were consistent with experimental data, these d(Zn-Mn_{1st}) values do not match available experimental distances for tetrahedral (3.33 – 3.39 Å) and octahedral (3.50 –3.53 Å) Zn. Therefore, the mixed-occupancy structure may not occur in nature. On the other hand, Manceau et al. (2002) reported single-shell EXAFS analyses for synthetic Zn-birnessites containing both tetrahedral and octahedral Zn in which d(Zn-Mn_{1st}) was 3.45-3.48 Å. This range, which applies to an approximately 1:3 mixture of the two Zn

coordination environments, is close to our average d(Zn-Mn_{1st}) for both Zn^{IV}-TCS + Zn^{VI}-TCS (3.42 Å) and a 1:1 mixture of Zn^{IV}-TCS + Zn^{IV}-TCS plus Zn^{VI}-TCS + Zn^{VI}-TCS (3.43 Å).

4. CONCLUSIONS

Our DFT study provides insight into the occurrence of Zn^{IV} and Zn^{VI} surface complexes at Mn vacancies in hexagonal birnessite, demonstrating that Zn^{IV} forms stronger chemical bonds with O of a Mn(IV) vacancy site than Zn^{VI} does. This is consistent with experimental observations of the predominance of Zn^{IV}-TCS at low loading of sorbed Zn in birnessite. On the other hand, the calculated total electronic energy of Zn^{IV}-TCS MnO_2, which is lower than but close to that of Zn^{VI}-TCS MnO_2 (11.6 kJ/mol difference), indicates that Zn^{IV}-TCS and Zn^{VI}-TCS surface complexes both can occur in birnessite interlayers, as observed experimentally, despite the difference in bond strength of Zn. Comparison between $ZnMn_3O_7{\cdot}3H_2O$ and $ZnMn_3O_7{\cdot}H_2O$, which have a high Zn/Mn ratio, suggests that occurrence of Zn^{VI}-TCS along with Zn^{IV}-TCS in hexagonal birnessite may be more related to Zn-birnessite stability mediated by interactions of Zn ions (e.g., through H-bonding) with neighboring Zn ions or with adjacent Mn octahedral sheets than to the existence of Mn(III) substitution and Zn bond-strength difference. A direct calculation of the relative stability would require the inclusion not only of quantum zero-point energy but also of additional thermally disordered water of hydration and the computation of accurate free energies, which lies beyond the scope of this paper.

Our geometry-optimization based on DFT has also enabled us to explore structural relaxation around Mn vacancies, a difficult task for current experimental techniques. The detailed structures of isolated Zn-TCS species and Mn vacancies in hexagonal Mn(IV)O_2

obtained by our DFT study can serve as fully-characterized end-member species of Zn-TCS to facilitate the interpretation of spectroscopic data on Zn sorbed in birnessite and thus help to achieve accurate modeling of the fate of Zn in terrestrial and aquatic environments.

ACKNOWLEDGMENTS

This research reported in this paper was supported by the Director, Office of Energy Research, Office of Basic Energy Sciences, of the U.S. Department of Energy under Contract No. DE-AC02-05CH11231. Our computations used resources of the National Energy Research Scientific Computing Center, which is supported by the Office of Science of the U.S. Department of Energy under contract No. DE-AC02-05CH11231. We also acknowledge the use of the SCARF computing facilities at STFC Rutherford Appleton Laboratory.

REFERENCES

Balachandran D., Morgan D., Ceder G., and van de Walle A. (2003) First-principles study of the structure of stoichiometric and Mn-deficient MnO_2. *J. Solid State Chem.* **173**, 462-475.

Clark S. J., Segall M. D., Pickard, C. J., Hasnip, P. J., Probert, M. J., Refson, K., and Payne, M.C. (2005) First principles methods using CASTEP. *Z. Kristallogr.* **220**, 567-570.

Cline J. A., Rigos A. A., and Arias T. A. (2000) Ab initio study of magnetic structure and chemical reactivity of Cr_2O_3 and its (0001) surface. *J. Phys. Chem. B* **104**, 6195-6201.

Cohen A. J. and Gordon R. G. (1976) Modified electron-gas study of stability, elastic properties, and high-pressure behavior of MgO and CaO crystals. *Phys. Rev. B* **14**, 4593-4605.

Cramer C. J. (2003) *Essentials of Computational Chemistry*. John Wiley & Sons Ltd, Chichester.

Dudev T. and Lim C. (2000) Tetrahedral vs octahedral zinc complexes with ligands of biological interest: A DFT/CDM study. *J. Am. Chem. Soc.* **122**, 11146-11153.

Franchini C., Podloucky R., Paier J., Marsman M., and Kresse G. (2007) Ground-state properties of multivalent manganese oxides: Density functional and hybrid density functional calculations. *Phys. Rev. B* **75**, 195128-11.

Gaillot A. C., Flot D., Drits V. A., Manceau A., Burghammer M., and Lanson B. (2003) Structure of synthetic K-rich birnessite obtained by high-temperature decomposition of $KMnO_4$. I. Two-layer polytype from 800 °C experiment. *Chem. Mater.* **15**, 4666-4678.

Gallego S., Beltrán J. I., Cerdá J., and Muñoz M. C. (2005) Magnetism and half-metallicity at the O surfaces of ceramic oxides. *J. Phys. Condens. Matter* **17**, L451-L457.

Isaure M. P., Manceau A., Geoffroy N., Laboudigue A., Tamura N., and Marcus M. A. (2005) Zinc mobility and speciation in soil covered by contaminated dredged sediment using micrometer-scale and bulk-averaging X-ray fluorescence, absorption and diffraction techniques. *Geochim. Cosmochim. Acta* **69**, 1173-1198.

Johnson E. A. and Post J. E. (2006) Water in the interlayer region of birnessite: Importance in cation exchange and structural stability. *Am. Mineral.* **91**, 609-618.

Kanamori J. and Terakura I. (2001) A general mechanism underlying ferromagnetism in transition metal compounds. *J. Phys. Soc. Jpn.* **70**, 1433-1434.

Kim S. H., Kim S. J., and Oh S. M. (1999) Preparation of layered MnO_2 via thermal decomposition of $KMnO_4$ and its electrochemical characterizations. *Chem. Mater.* **11**, 557-563.

Koch W. and Holthausen M. C. (2002) *A Chemist's Guide to Density Functional Theory*. Wiley-VCH, New York.

Kohanoff J. (2006) *Electronic Structure Calculations for Solids and Molecules: Theory and Computational Methods*. University Cambridge Press, Cambridge.

Kohn W. and Sham L. J. (1965) Self-consistent equations including exchange and correlation effects. *Phys. Rev.* **140**, A1133-A1138.

Kresse G. and Furthmüller J. (1996) Efficient iterative schemes for ab initio total-energy calculations using a plane-wave basis set. *Phys. Rev. B* **54**, 11169-11186.

Lanson B., Drits V. A., Gaillot A. C., Silvester E., Plancon A., and Manceau A. (2002) Structure of heavy-metal sorbed birnessite: Part 1. Results from X-ray diffraction. *Am. Mineral.* **87**, 1631-1645.

Lanson B., Marcus M. A., Fakra S., Panfili F., Geoffroy N., and Manceau A. (2008) Formation of Zn-Ca phyllomanganate nanoparticles in grass roots. *Geochim. Cosmochim. Acta*, **72**, 2478-2490.

Manceau A., Lanson B., and Drits V. A. (2002) Structure of heavy metal sorbed birnessite. Part III: Results from powder and polarized extended X-ray absorption fine structure spectroscopy. *Geochim. Cosmochim. Acta* **66**, 2639-2663.

Manceau A., Lanson M., and Geoffroy N. (2007) Natural speciation of Ni, Zn, Ba, and As in ferromanganese coatings on quartz using X-ray fluorescence, absorption, and diffraction. *Geochim. Cosmochim. Acta* **71**, 95-128.

Marcus M. A., Manceau A., and Kersten M. (2004) Mn, Fe, Zn and As speciation in a fast-growing ferromanganese marine nodule. *Geochim. Cosmochim. Acta* **68**, 3125-3136.

Martin R. M. (2004) *Electronic Structure: Basic Theory and Practical Methods*. Cambridge University Press, Cambridge.

Mattsson A. E., Schultz P. A., Desjarlais M. P., Mattsson T. R., and Leung K. (2005) Designing meaningful density functional theory calculations in materials science–a primer. *Model. Simul. Mater. Sci. Eng.* **13**, R1-R31.

Milman V., Winkler B., White J. A., Pickard C. J., Payne M. C., Akhmatskaya, E. V., and Nobes, R. H. (2000) Electronic structure, properties, and phase stability of inorganic crystals: A pseudopotential plane-wave study. *Int. J. Quantum Chem.* **77**, 895-910.

Mishra S. K. and Ceder G. (1999) Structural stability of lithium manganese oxides. *Phys. Rev. B* **59**, 6120-6130.

Miyata N., Tani Y., Sakata M., and Iwahori K. (2007) Microbial manganese oxide formation and interaction with toxic metal ions. *J. Biosci. Bioeng.* **104**, 1-8.

Monkhorst H. J. and Pack J. D. (1976) Special points for Brillouin-zone integrations. *Phys. Rev. B* **13**, 5188-5192.

Moessner R. and Ramirez A. R. (2006) Geometrical frustration. *Physics Today* **59**, 24-29.

Mulliken R. S. (1955) Electronic population analysis on LCAO-MO molecular wave functions. I. *J. Chem. Phys.* **23**, 1833-1840.

Pask J. E., Singh D. J., Mazin I. I., Hellberg C. S., and Kortus J. (2001) Structural, electronic, and magnetic properties of MnO. *Phys. Rev. B* **64**, 024403.

Payne M. C., Teter M. P., Allan,D. C., Arias T. A., and Joannopoulos J. D. (1992) Iterative minimization techniques for *ab initio* total-energy calculations: molecular-dynamics and conjugate gradients. *Rev. Mod. Phys.* **64**, 1045-1097.

Perdew J. P., Burke K., and Ernzerhof M. (1996) Generalized gradient approximation made simple. *Phys. Rev. Lett.* **77**, 3865-3868.

Pfrommer B. G., Cote M., Louie S. G., and Cohen M. L. (1997) Relaxation of crystals with the quasi-Newton method. *J. Comput. Phys.* **131**, 233-240.

Post J. E. and Appleman D. E. (1988) Chalcophanite, $ZnMn_3O_7 \cdot 3H_2O$ - New crystal-structure determinations. *Am. Mineral.* **73**, 1401-1404.

Probert M. I. J. (2003) Improved algorithm for geometry optimisation using damped molecular dynamics. *J. Comput. Phys.* **191**, 130-146.

Probert M. I. J. and Payne M. C. (2003) Improving the convergence of defect calculations in supercells: An *ab initio* study of the neutral silicon vacancy. *Phys. Rev. B* **67**, 075204.

Segall M. D., Lindan P. J. D., Probert M. J., Pickard C. J., Hasnip,P. J., Clark S. J., and Payne M. C. (2002) First-principles simulation: ideas, illustrations and the CASTEP code. *J. Phys. Condens. Matter* **14**, 2717-2744.

Segall, M. D., Shah, R., Pickard, C. J., and Payne, M. C. (1996) Population analysis of plane-wave electronic structure calculations of bulk materials. *Phys. Rev. B* **54**, 16317-16320.

Singh, D. J. (1997) Magnetic and electronic properties of $LiMnO_2$. *Phys. Rev. B* **55**, 309-312.

Tebo B. M., Bargar J. R., Clement B. G., Dick G. J., Murray K. J., Parker D., Verity R., and Webb S. M. (2004) Biogenic manganese oxides: Properties and mechanisms of formation. *Annu. Rev. Earth Planet. Sc.* **32**, 287-328.

Toner B., Manceau A., Webb S. M., and Sposito G. (2006) Zinc sorption to biogenic hexagonal-birnessite particles within a hydrated bacterial biofilm. *Geochim. Cosmochim. Acta* **70**, 27-43.

Tonkin J. W., Balistrieri L. S., and Murray J. W. (2004) Modeling sorption of divalent metal cations on hydrous manganese oxide using the diffuse double layer model. *Appl. Geochem.* **19**, 29-53.

Vanderbilt D. (1990) Soft self-consistent pseudopotentials in a generalized eigenvalue formalism. *Phys. Rev. B* **41**, 7892-7895.

Villalobos M., Bargar J., and Sposito G. (2005) Mechanisms of Pb(II) sorption on a biogenic manganese oxide. *Environ. Sci. Technol.* **39**, 569-576.

Villalobos M., Lanson B., Manceau A., Toner B., and Sposito G. (2006) Structural model for the biogenic Mn oxide produced by *Pseudomonas putida*. *Am. Mineral.* **91**, 489-502.

Zhao J. L., Zhang W. Q., Li X. M., Feng J. W., and Shi X. (2006) Convergence of the formation energies of intrinsic point defects in wurtzite ZnO: first-principles study by projector augmented wave method. *J. Phys. Condens. Matter* **18**, 1495-1508.

Figure Captions

Fig. 1. Geometry-optimized structures of Zn complexes and Mn octahedra in $ZnMn_3O_7 \cdot 3H_2O$ (chalcophanite), viewed perpendicularly to (a) the *c*-axis and (b) the *ab* plane (Red: O; White: H; Teal: Zn; Purple octahedron: Mn(IV) octahedron). Interatomic distances, H-bond distances (dotted lines), and sheet thickness are given in Å. H_2O molecules are omitted for visual clarity in (b). Double-headed arrow in (b) indicates the distance between nearest-neighbor Mn (Mn_{1st}) and Zn. Gray octahedra represent Mn_{1st} ones from Zn. The labels O1 and O3 identify O bonded to three Mn (O_{3Mn}), whereas O2 identifies O bonded to two Mn and one Zn (O_{2Mn}) (See Table 2 for their coordinates).

Fig. 2. Geometry-optimized isolated Zn^{IV}-TCS in 4x4x1 supercell $Mn(IV)O_2$ (11.587 Å x 11.587 Å x 14.001 Å), viewed perpendicularly to (a) the *c*-axis and (b) the *ab* plane. Labeling and color scheme is the same as in Fig. 1. Double-headed arrows in (b) indicate interatomic distances in Å. Mn_{2nd}: Mn second-nearest to Zn; O_{2Mnx}: O bonded to two Mn but no H or Zn.

Fig. 3. Geometry-optimized (a) isolated Zn^{IV}-TCS that has H-bonds with two H_2O and (b) isolated Zn^{VI}-TCS. Labeling and color scheme is the same as in Fig. 1. Values in parentheses are electron overlap population in Zn-O_{2Mn} bond.

Fig. 4. View of a vacancy in the *ab* plane (Zn and H_2O molecules omitted for visual clarity) of (a) constrained Zn^{VI}-TCS + Zn^{VI}-TCS with atomic coordinates for MnO_2 fixed (see text), (b) Zn^{VI}-TCS + Zn^{VI}-TCS with the coordinates for MnO_2 relaxed, and (c) Zn^{IV}-TCS + Zn^{IV}-TCS

with the coordinates for MnO_2 relaxed. Labeling and color scheme is the same as in Fig. 1. Single-headed arrows in (a) represent the directions of Mn and O displacements upon structural relaxation. Double-headed arrows denote $d(Mn_{1st}\text{-}Mn_{1st})$, $d(O\text{-}O_{Mn1st})$, and $d(O\text{-}O_{vac})$ in Å. In the (a) constrained Zn^{VI}-TCS + Zn^{VI}-TCS, $d(Mn_{1st}\text{-}Mn_{1st})$ = 2.90 Å and $d(O\text{-}O_{Mn1st})$ and $d(O\text{-}O_{vac})$ both equal 2.54 Å.

Fig. 5. Charge densities of ions relative to the corresponding neutral atoms, section taken parallel to the *ac* plane in (a) Zn^{IV}-TCS + Zn^{IV}-TCS, (b) Zn^{VI}-TCS + Zn^{VI}-TCS, and (c) mixed Zn^{IV}-TCS + Zn^{VI}-TCS. (Red: O; White: H; Teal: Zn; Purple: Mn). Blue areas represent electron-depleted regions and red areas represent electron-rich regions. Solid arrows indicate d(Zn-□-Zn), while dotted arrows indicate $d(Zn\text{-}Mn_{1st})$, both in Å.

Fig. 1

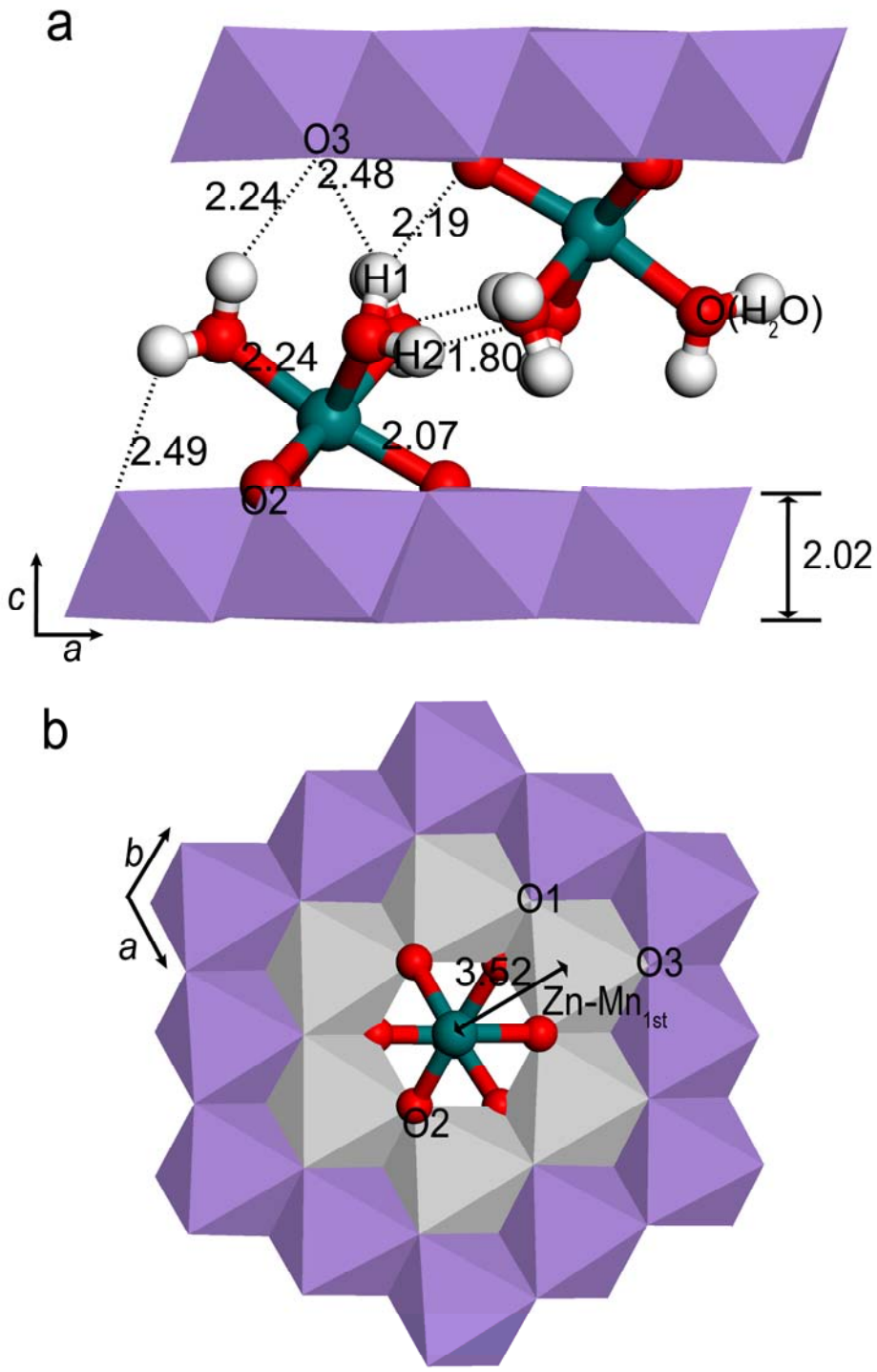
a
O3
2.48
2.24
2.19
H1
O(H2O)
2.24
H2
1.80
2.07
2.49
O2
2.02
c
a
b
b
a
O1
3.52
O3
Zn-Mn1st
O2

Fig. 2

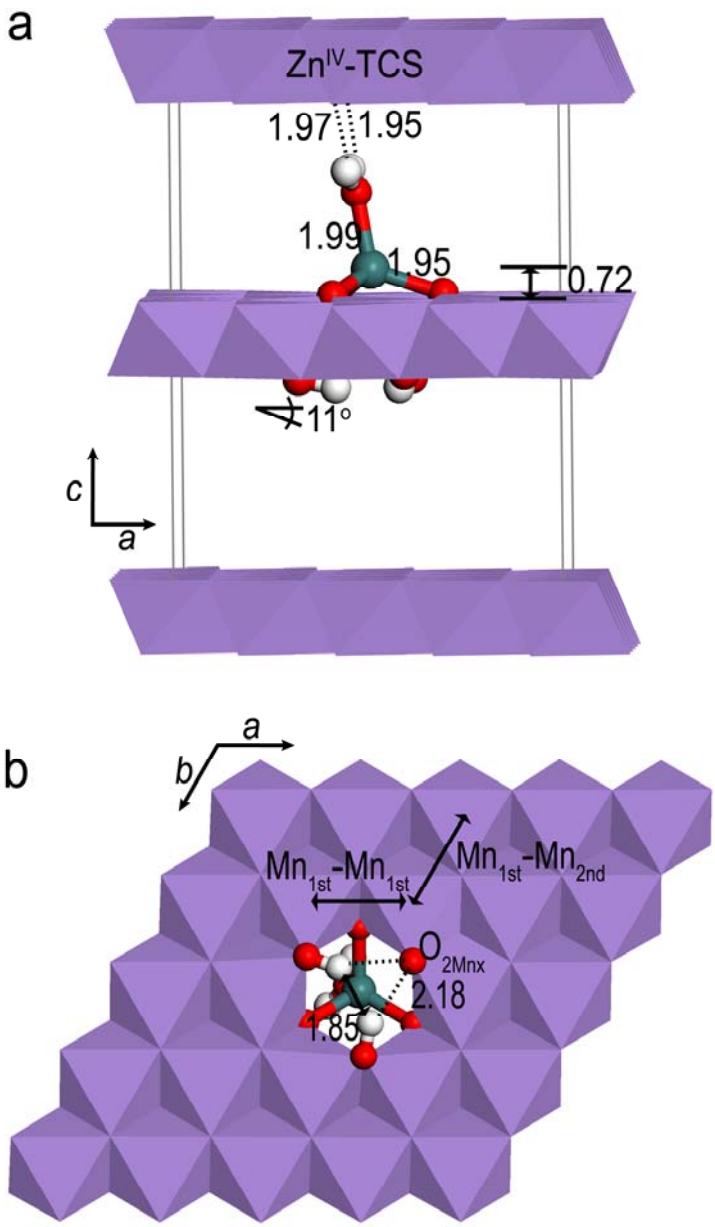
a
Zn^{IV}-TCS
1.97
1.95
1.99
1.95
0.72
11°
c
a
b
a
b
Mn$_{1st}$-Mn$_{1st}$
Mn$_{1st}$-Mn$_{2nd}$
O$_{2Mnx}$
2.18
1.85

Fig. 3

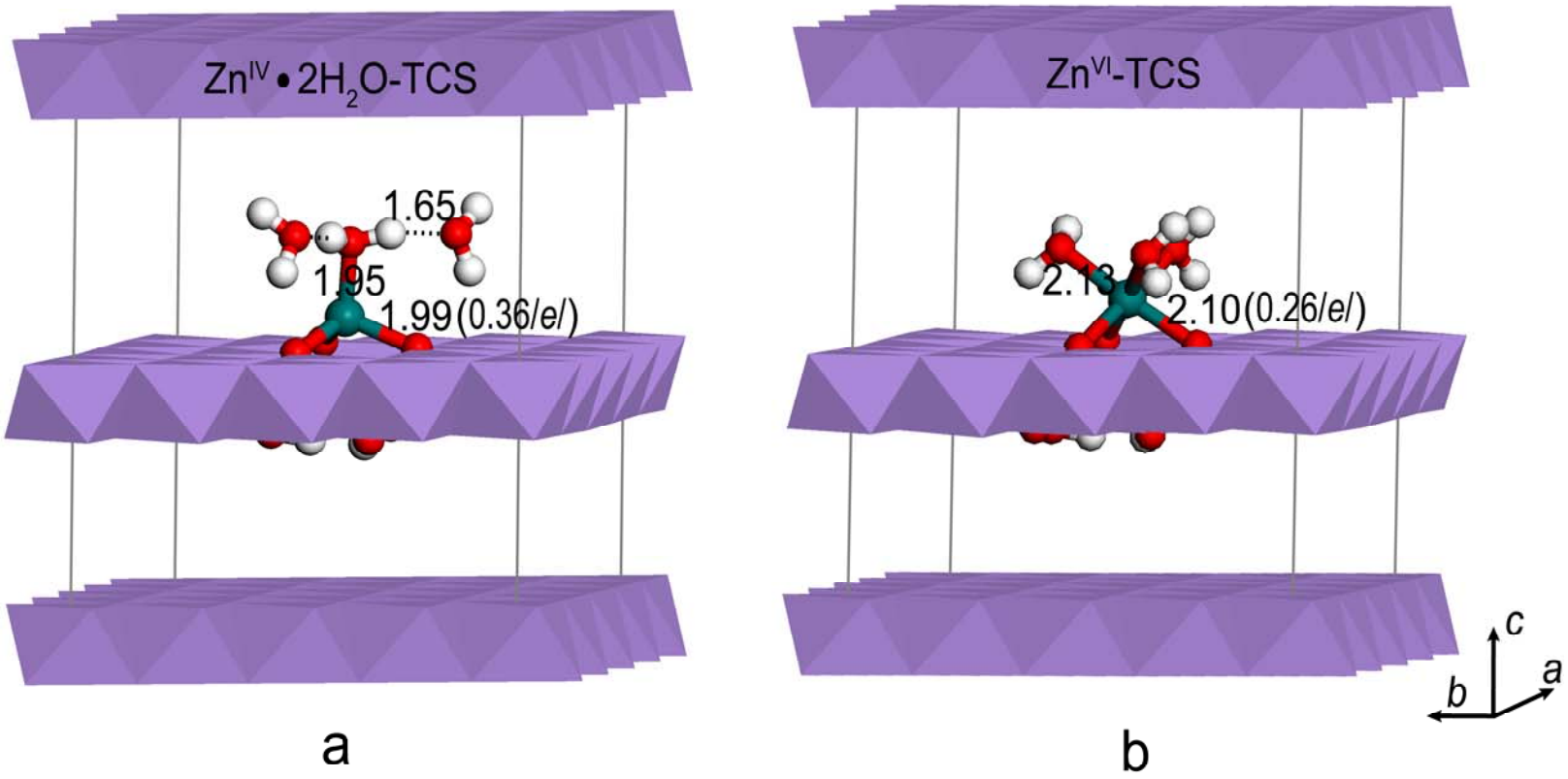

Fig. 4

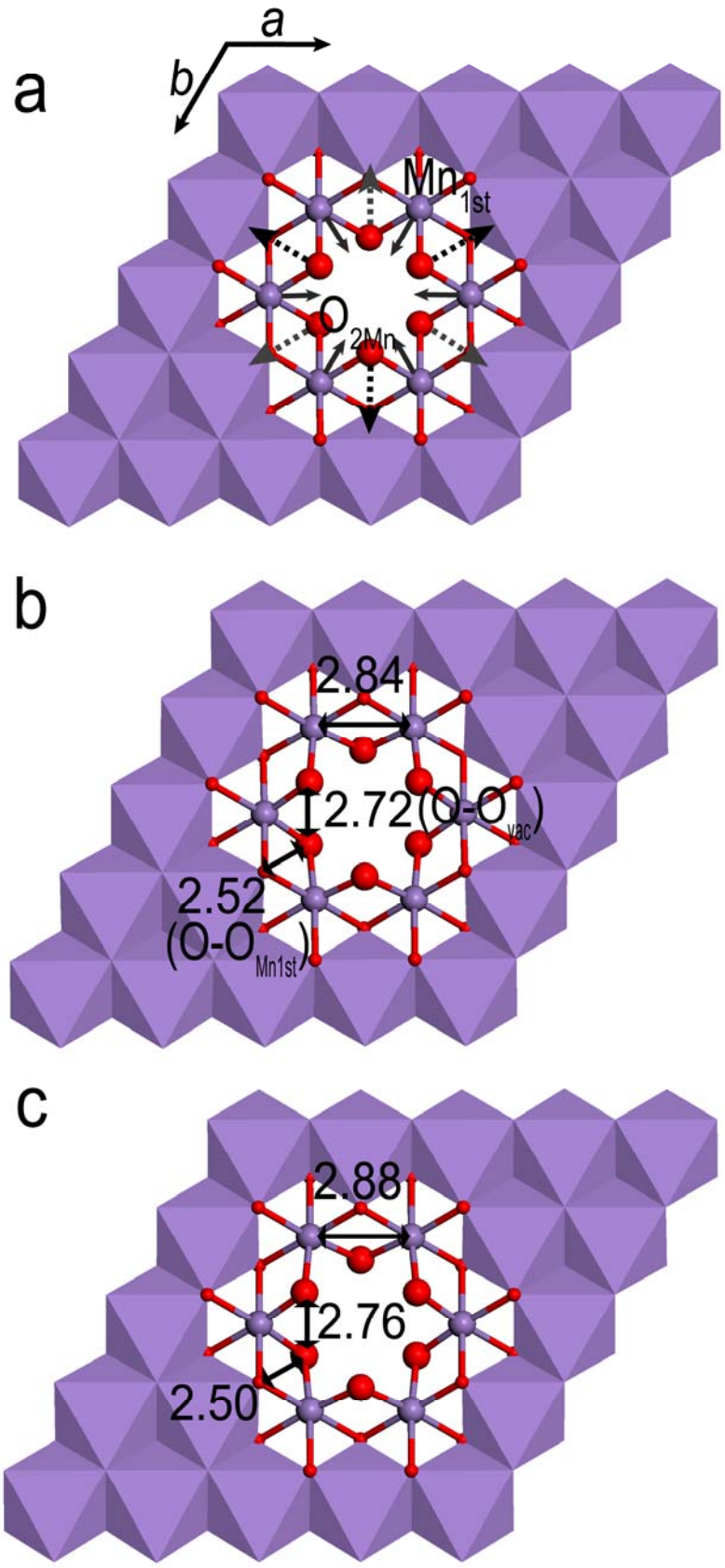

Fig. 5

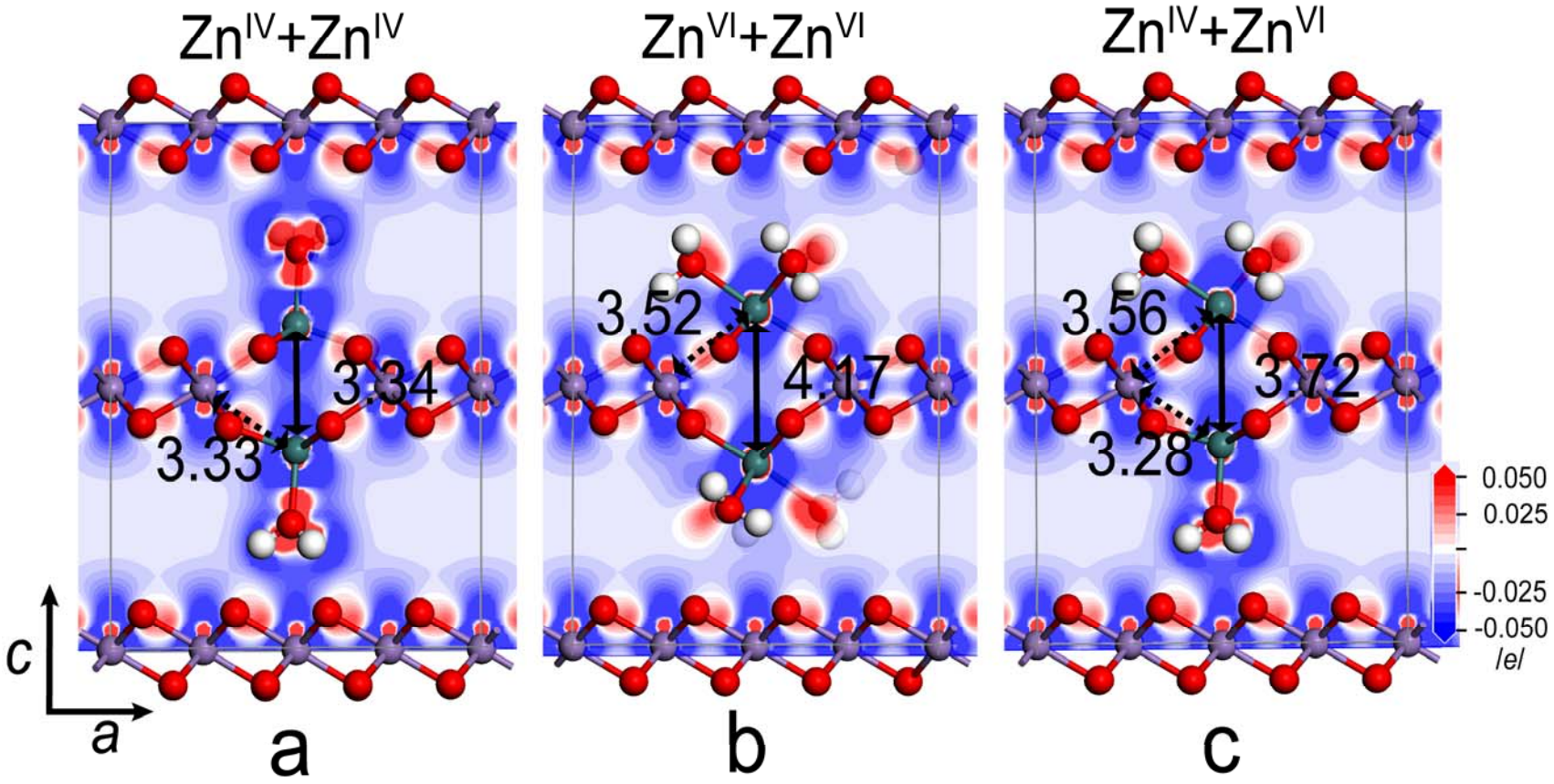
Zn^IV+Zn^IV
Zn^VI+Zn^VI
Zn^IV+Zn^VI
3.34
3.33
3.52
4.17
3.56
3.72
3.28
0.050
0.025
-0.025
-0.050
/e/
c
a
a
b
c

Table 1. Structural parameters for tetrahedrally-coordinated Zn (Zn^{IV}) triple-corner-sharing surface complexes in birnessite samples.

Atom pair	ZnBi8[a]		Marine nodule[b]		Zn biomn1[c]		Zn δ-MnO_2[d]		6KR[e]		Plant roots[f]	
	R (Å)	*N*	*R* (Å)	*N*	*R* (Å)	*N*	*R* (Å)	*N*	*R* (Å)	*N*	*R* (Å)	*N*
Zn-O	1.97	3.3	1.96 (±0.02)	4.9 (±1.0)	1.97 (±0.01)	4.4 (±0.7)	2.07 (±0.02)	5.7 (±1.1)	n.r.	n.r.	n.r.	n.r.
Zn-Mn_{1st}	3.35[g]	2.9	3.33 (±0.02)	6.7 (±1.3)	3.36 (±0.03)	5.7 (±1.0)	3.39* (±0.02)	1.8* (±0.4)	n.r.	n.r.	n.r.	n.r.

R: Interatomic distance determined by EXAFS analysis; *N*: Number of nearest-neighbor atoms; n.r.: not reported.

*Result of double-shell EXAFS analysis.

[a] Synthetic Zn-birnessite (Manceau et al., 2002), structure and Zn^{IV} content based on spectra of ZnO and chalcophanite.

[b] Natural marine Zn-birnessite (Marcus et al., 2004), based on spectra of ZnBi8[a] and chalcophanite.

[c] Bacteriogenic Zn-birnessite (Toner et al., 2006), based on spectra of ZnBi8[a].

[d] Zn δ-MnO_2 (Toner et al., 2006), based on spectra of biomn1[c] and chalcophanite.

[e] Birnessite coating (Manceau et al., 2007), based on spectra of ZnBi8[a] and marine nodule[b] sample.

[f] Zn-Mn coprecipitate on plant roots (Lanson et al., 2008), based on spectra of 6KR[e], chalcophanite, and Zn δ-MnO_2[d].

[g] Result of double-shell EXAFS analysis; result of single-shell analysis is 3.37 Å (Marcus et al, 2004).

Table 2. Atomic coordinates in geometry-optimized $ZnMn_3O_7 \cdot 3H_2O$ (chalcophanite).

Element	DFT			XRD[a]		
	X	*Y*	*Z*	*X*	*Y*	*Z*
Zn	0	0	0.09779	0	0	0.09998
Mn	0.71868	0.57786	0.99951	0.71869	0.57771	0.99948
O1	0.52758	0.62229	0.04566	0.52785	0.62298	0.04721
O2	0.25877	0.20499	0.04973	0.26078	0.20656	0.05048
O3	0	0	0.71235	0	0	0.71250
O4	0.17259	0.92092	0.16665	0.17901	0.93108	0.16435
H1	0.183	0.972	0.210	0.229[b]	0.025[b]	0.198[b]
H2	0.316	0.962	0.157	0.310[b]	0.940[b]	0.144[b]

O1, O3: O bonded to three Mn (O_{3Mn}); O2: O bonded to one Zn and two Mn (O_{2Mn}); O4: O of H_2O. The optimized cell parameters were a =7.602 Å and c = 21.349 Å.

[a] Rietveld refinement of Bisbee chacophanite whose cell parameters are a = 7.533 Å and c = 20.794 Å (Post and Appleman, 1988).

[b] Post and Appleman (1988) calculated H coordinates using a potential-energy function evaluated at the fixed atomic positions (Zn, Mn, O) of the Bisbee chalcophanite structure obtained from XRD refinement.

Table 3. Interatomic distances (Å) in geometry-optimized isolated Zn^{IV}-TCS and Zn^{VI}-TCS.

Atom pair	DFT			EXAFS[c]	
	Zn^{IV}	Zn^{IV}•$2H_2O$[a]	[b]Zn^{VI}	Zn^{IV}-TCS	N[d]
Zn-O_{2Mn}	1.94	1.99	2.10		
	1.94	1.98	2.10		
	1.95	1.95	2.12		
Zn-O (H_2O)	1.99	1.95	2.13		
			2.13		
			2.16		
	<1.96>	<1.97>	<2.12>	1.962 ± 0.015	4.9
Zn-Mn_{1st}	3.30	3.41	3.58		
	3.35	3.42	3.57		
	3.37	3.37	3.56		
	3.36	3.41	3.56		
	3.34	3.34	3.56		
	3.30	3.38	3.55		
	<3.34>	<3.39>	<3.56>	3.33 ± 0.02	6.7
Mn-Mn	2.83 – 2.93	2.82 – 2.94	2.82 – 2.96	2.89 ± 0.007	4.4

O_{2Mn}: surface O at a vacancy site bonded to two Mn; Mn_{1st}: nearest Mn to Zn. N: number of nearest-neighbor atoms. Values in < > are averages for d(Zn-O) and d(Zn-Mn_{1st}).

[a] Tetrahedral Zn with H-bonding to two H_2O (See Fig. 3a).

[b] Octahedral Zn (See Fig. 3b).

[c] EXAFS single-shell results for marine Zn-birnessite (Marcus et al., 2004), in which octahedrally-coordinated Zn is at most 7 mol %.

[d] Error in N is ± 20 %.

Table 4. Interatomic distances (Å) in three types of geometry-optimized, doubly-occupied Zn-TCS Mn(IV)O_2.

Atom pair	Tetrahedral Zn		Octahedral Zn		Mixed Zn	
	Zn^{IV}-TCS	Zn^{IV}-TCS	Zn^{VI}-TCS	Zn^{VI}-TCS	Zn^{IV}-TCS	Zn^{VI}-TCS
Zn-O_{2Mn}	1.94	1.94	2.08	2.09	1.94	2.09
	1.94	1.94	2.10	2.09	1.94	2.10
	1.94	1.94	2.13	2.12	1.95	2.13
Zn-O (H_2O)	1.99	2.00	2.13	2.13	2.01	2.13
			2.14	2.13		2.13
			2.17	2.18		2.16
	<1.95>	<1.96>	<2.13>	<2.12>	<1.96>	<2.12>
Zn-Mn_{1st}	3.32	3.32	3.51	3.51	3.28	3.54
	3.32	3.32	3.51	3.51	3.28	3.55
	3.33	3.33	3.52	3.52	3.28	3.55
	3.33	3.33	3.53	3.52	3.28	3.57
	3.33	3.33	3.55	3.54	3.28	3.58
	3.33	3.33	3.55	3.54	3.28	3.58
	<3.33>	<3.33>	<3.53>	<3.52>	<3.28>	<3.56>
Mn_{1st}-Mn_{1st}	2.88		2.84		2.88[a]	2.85[b]

Values in < > are averages for *d*(Zn-O) and *d*(Zn-Mn_{1st}).

[a] Distance between Mn_{1st} octahedra whose shared O_{2Mn} are coordinated with Zn^{IV}-TCS

[b] Distance between Mn_{1st} octahedra whose shared O_{2Mn} are coordinated with Zn^{VI}-TCS